Soft Matter

Toroidal nuclei of columnar lyotropic chromonic liquid crystals coexisting with isotropic phase.

Journal:	*Soft Matter*
Manuscript ID	SM-ART-05-2022-000712.R1
Article Type:	Paper
Date Submitted by the Author:	16-Jul-2022
Complete List of Authors:	Koizumi, Runa; Kent State university, Chemical Physics Interdisciplinary Program and Liquid crystal institute Golovaty, Dmitry; University of Akron Buchtel College of Arts and Sciences, Mathematics Alqarni, Ali; Kent State university, Chemical Physics Interdisciplinary Program and Liquid crystal institute Walker, Shawn; Louisiana State University, Mathematics Nastishin, Yuriy; Kent State University, Liquid Crystal Institute; Institute of Physical Optics, Calderer, Maria-Carme; University of Minnesota Twin Cities, Mathematics Lavrentovich, Oleg; Kent State university, Chemical Physics Interdisciplinary Program and Liquid crystal institute

TOROIDAL NUCLEI OF COLUMNAR LYOTROPIC CHROMONIC LIQUID CRYSTALS COEXISTING WITH ISOTROPIC PHASE

RUNA KOIZUMI, DMITRY GOLOVATY, ALI ALQARNI, SHAWN W. WALKER, YURIY A. NASTISHIN, M. CARME CALDERER, AND OLEG D. LAVRENTOVICH

Abstract. Nuclei of ordered materials emerging from the isotropic state usually show a shape topologically equivalent to a sphere; the well-known examples are crystals and nematic liquid crystal droplets. In this work, we explore experimentally and theoretically the nuclei of columnar lyotropic chromonic liquid crystal coexisting with the isotropic phase that are toroidal in shape. The geometry of toroids depends strongly on the molecular concentrations and presence of a crowding agent, polyethylene glycol. High concentrations result in thick toroids with small central holes, while low concentrations yield thin toroids with wide holes. The multitude of the observed shapes is explained by the balance of bending elasticity and anisotropic interfacial tension.

1. Introduction

Surface tension defines the shapes of finite-size condensed matter. Tiny droplets of water in air are spherical to minimize their surface area, while solid crystals have facets due to orientational dependence of surface tension. Bulk interactions are irrelevant here: too weak to resist surface tension in the first example or too strong to permit internal curvatures in the second example. Liquid crystals show a more delicate balance between the bulk and surface energies yielding rich morphology of droplet shapes, such as smectic "batonnets" [1], nematic spindle-like tactoids [2], branched [3, 4] and dividing droplets [5]. Although liquid crystal droplets are typically topologically equivalent to a sphere, here we explore toroidal droplets that form when a columnar liquid crystal with two-dimensional positional ordering coexists with its own isotropic melt [6].

The studied material is a lyotropic chromonic liquid crystal (LCLC) formed by plank-like molecules of disodium chromoglycate (DSCG) with hydrophobic polyaromatic cores and hydrophilic peripheries [7, 8, 9, 10, 11]. When dispersed in water, the molecules form cylindrical aggregates by stacking face-to-face, Fig. S1. Chromonic self-assembly is common for a broad family of materials, including nucleotides, dyes, food colorants, proteins, and pharmaceuticals, such as the anti-asthmatic and antiallergy drug disodium cromoglycate (DSCG). At sufficiently high concentrations, the aggregates align parallel to each other forming a nematic (N) phase. At still higher concentrations, the aggregates arrange into a hexagonal lattice producing a columnar (Col) phase, Fig. S1 [8, 9].

Phase transitions in LCLCs are controlled by both temperature and concentration. The isotropic (I)-Col phase transition exhibits a broad coexistence region in which Col nuclei are shaped as solid toroids [6] or spool-like structures in which the central hole shrinks into a singular line [12]. These shapes resemble condensed nanoscale toroids of DNA strands in viral capsids [13, 14, 15, 16, 17, 18] albeit at much larger length scales of tens of micrometers [12, 6] accessible to optical microscopy. The molecules within chromonic aggregates are bound by weak noncovalent forces so that chromonic aggregates can intersect, reconnect and exchange ends, avoiding entanglements known for DNA strands.

In this work, we demonstrate that the toroidal shape of Col nuclei in the biphasic Col+I region of water dispersions of DSCG depends strongly on the concentrations c of DSCG and C of a condensing agent polyethylene glycol (PEG). PEG partitions into the I phase and helps to condense the Col phase [6]. The increase of c and C yields larger toroids with narrow central holes and pronounced facets clearly revealed when the nuclei in a shape of handles are attached to the bounding glass plates. The observed shapes are explained by the balance of bend elasticity, defined by the bend modulus K_3, and the interfacial Col-I energy

with a surface tension $\sigma_{\|}$. A dimensionless parameter $\beta = K_3/\left(\sigma_{\|}V^{1/3}\right)$ measures the ratio of bending to interfacial energy and determines the shape of the cross-section of the toroidal aggregate. Orientational dependence of the interfacial tension on translations **u** within the hexagonal lattice produces faceted toroids. The equilibrium toroid is thin with a wide central hole when $\beta \gg 1$; for $\beta \ll 1$, the central hole shrinks dramatically, and the toroids resemble a faceted sphere. We first present the experimental data and then the mathematical model.

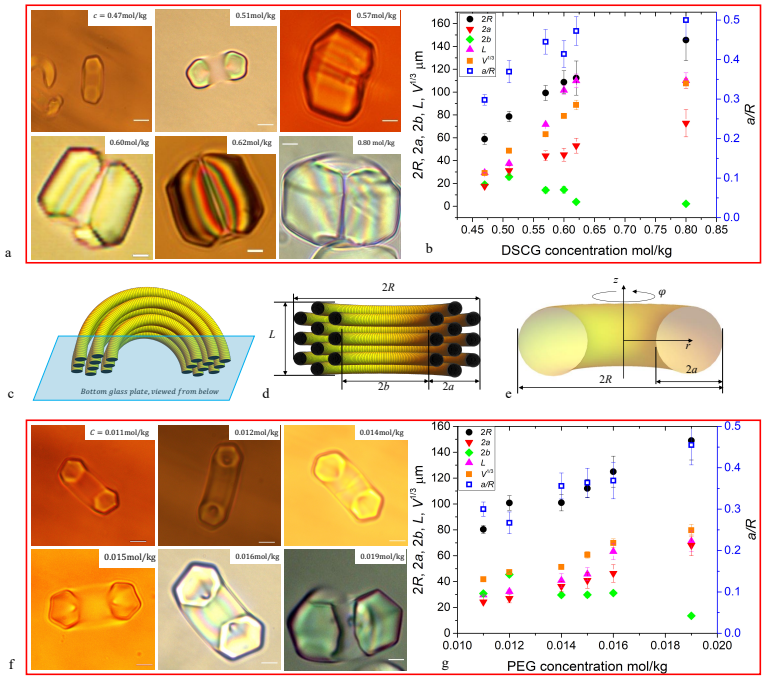

FIGURE 1. (a) Optical microscopy textures of half-toroids at different concentrations of DSCG: c=0.47, 0.51, 0.57, 0.60, 0.62, 0.80 mol/kg, scale bars 20μm. (b) The ratio a/R (right axis, blue open square), maximum width $2R$, "thickness" of the toroidal cross-section $2a$, maximum opening $2b$ of the central hole, and the measure of volume $V^{\frac{1}{3}}$ as functions of c. Here $T = 45°$C. (c) Scheme of the Col half-torus attached as a handle to the bottom glass substrate of the flat capillary; (d) Shape characteristics measured in the experiment; (e) Geometry of the toroid used in the analysis of the shape dependency on the material parameters. (f) Microscope images of half-toroids formed at different concentrations C of PEG added to DSCG of a fixed concentration $c = 0.34$ mol/kg: $C = 0.011$, 0.012, 0.014, 0.015, 0.016, 0.019 mol/kg. Scale bars 20μm. (g) The ratio a/R (right axis, blue open square), maximum width $2R$, "thickness" of the toroidal cross-section $2a$, maximum opening $2b$ of the central hole, and the measure of volume $V^{\frac{1}{3}}$, all plotted as a function of C. Here $T = 42°$C.

2. EXPERIMENT.

2.1. **Toroids in aqueous DSCG and DSCG+PEG solutions**

The Col nuclei appear upon cooling from the I phase as thin flexible filaments that bend into toroids, Fig. S2, to prevent the contact of open ends with the I phase, see Supplementary Material. Their shape depends on the concentration c of DSCG, Fig. 1a,b and C of PEG, Fig. 1f,g. The nuclei are actually half-toroids with faceted cross-sections that are mostly attached to the bottom glass plate because of the homeotropic alignment of the director and gravity, Fig. 1c. In Fig. 1b,g we plot the concentration dependencies of the

maximum extension $2R$ of half-toroids along the normal to the axis of bend, minimum width of the central opening $2b$, maximum width $2a$ of the solid part of the toroid, maximum extension L of the toroid along the axis of bend, and the volume V of half-torus, plotted as $V^{\frac{1}{3}}$. All parameters, except for the hole width $2b$, increase with c and C. In pure DSCG, the hole width $2b$ decreases from $\approx 20\mu$m at $c = 0.47$ mol/kg to $\leq 1\mu$m at $c = 0.8$ mol/kg, Fig. 1b. The ratio a/R increases from ~0.3 to the maximum possible value 0.5, transforming the central hole into a singular +1 disclination coinciding with the axis of the toroid, Fig. 1a, $c = 0.62$ and 0.8 mol/kg. In the Col phase, this disclination is topologically stable [19] and features a submicron core of a radius a_c.

In condensates with a fixed at $c = 0.34$ mol/kg, addition of PEG at concentration $C > 0.011$ mol/kg causes phase separation into the Col and I phases, as confirmed by X-ray measurements [20]. The Col inclusions are toroids with cross-sections resembling hexagons, Fig. 1f. A distinct feature of DSCG+PEG system is that the central hole never shrinks into a disclination, as its smallest width $2b \approx 10\mu$m is relatively large, Fig. 1g.

It is important to stress that the homeotropic anchoring of Col aggregates at the glass substrate is not the reason for the existence of the facetted toroids, as these could be observed being freely suspended in very thick slabs, Fig. 2a,b. Among the freely-suspended shapes one can also observe compact domains, Fig. 2c, with two mutually perpendicular disclinations of strength 1/2, Fig. 2d. As suggested by Bouligand [21], the existence of two 1/2 mutually perpendicular disclinations proves the hexagonal order (six-fold symmetry) of the Col phase; these crossed configurations were previously observed by Oswald in the bulk of a thermotropic Col phase [22]. The six-fold symmetry is an important factor shaping the Col nuclei in the studied system, as detailed in the numerical analysis below. Since their orientation is fixed, half-toroids are easier to analyze than their full counterparts; this is why we present the shape parameters in Fig. 1 for half-toroids. Note finally that the homeotropic anchoring of LCLCs achieved in our study for the Col phase is not unique: a homeotropic alignment for the nematic phase of DSCG at a glass treated with N, N-dimethyl-N-octadecyl-3-aminopropyl trimethoxysilyl chloride (DMOAP) was reported by Nazarenko et. al. [23] and by Zhou et. al. [24], while Mushenheim et. al. [25] reported the effect for graphene-coated glass plates.

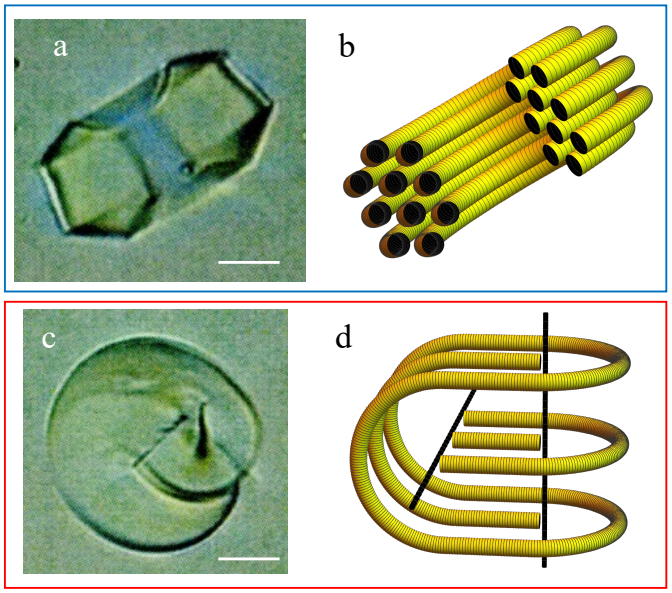

FIGURE 2. (a) Optical microscopy texture and (b) inner structure of a freely suspended facetted toroid; (c) Optical microscopy texture and (d) inner structure of a compact domain with two mutually perpendicular disclinations of strength 1/2. Scale bars 20 μm. Here $T = 50°$C; DSCG, $c = 0.55$ mol/kg.

2.2. **Elasticity-surface tension balance for thin toroids**

The toroidal shapes result from a balance of surface tension and bulk elasticity. To calculate the elastic energy of a toroid, we model it as a circular torus of a minor radius a and a major radius r, associated with the geometrical parameters in Fig. 1c as $r = R - a$, Fig. 1e. The elastic energy of half-torus is $F_e = \pi^2 K_3 \left(r - \sqrt{r^2 - a^2}\right)$, while the Col-I interfacial energy is $F_{s\|} = 2\pi^2 \sigma_\| ar$, where $\sigma_\|$ is the surface tension coefficient for tangential alignment of Col aggregates at the interface, assumed to be independent on the orientation of the hexagonal lattice. To enable analytical results, we consider thin toroids, $a \ll r$, in which case the surface energy at the Col-glass interface is insignificant as compared to $F_{s\|}$.

For $a \ll r$, the energy of the toroid simplifies to $F \approx \pi^2 K_3 r\xi/2 + 2\pi^2 \sigma_\| r^2 \sqrt{\xi}$, where $\xi = \frac{V}{\pi^2 r^3} \ll 1$. Minimizing F with respect to r, for a fixed volume $V = \pi^2 a^2 r = const$, one finds that $r = \left(\frac{V}{\pi^2}\right)^{\frac{1}{5}} \lambda_{ec}^{\frac{2}{5}}$, where we introduce the elastocapillary length $\lambda_{ec} = \frac{K_3}{\sigma_\|}$. The result leads to $a = \left(\frac{V}{\pi^2}\right)^{\frac{2}{5}} \lambda_{ec}^{-\frac{1}{5}}$ and

$$\frac{a}{r} = \frac{1}{\pi^{2/5} \beta^{3/5}}, \tag{1}$$

where

$$\beta = \frac{\lambda_{ec}}{V^{1/3}} = \frac{K_3}{\sigma_\| V^{1/3}} \tag{2}$$

is a dimensionless ratio of the bulk bend energy to the surface energy normalized by the characteristic size of the nuclei.

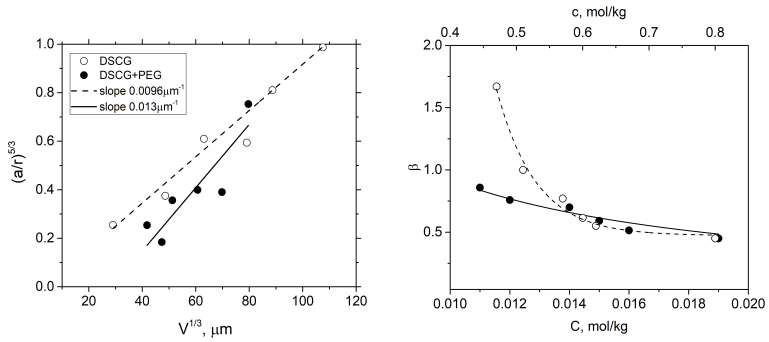

FIGURE 3. Geometrical parameters of toroids in DSCG and DSCG+PEG mixtures. (a) Aspect ratio measure of toroids $(a/r)^{\frac{5}{3}}$ is proportional to their characteristic size $V^{\frac{1}{3}}$; (b) the dimensionless parameter $\beta = K_3/\left(\sigma_\| V^{1/3}\right)$ decreases when the concentrations c and C increase; the curves are guide to an eye, although in the case of DECG+PEG, the curve is close to $\beta \propto 1/C$.

Eq. (1) confirms the qualitative trends observed experimentally in Figs. 1a,f, despite the limitation $a \ll r$, R imposed on the model. The concentration dependencies of the geometrical parameters in Figs. 1b,g show that a/r increases with V, in agreement with Eq. (1). The dependence of $(a/r)^{\frac{5}{3}}$ vs. $V^{\frac{1}{3}}$, Fig. 3a, is practically linear, which suggests that within the explored range of concentrations, the elastocapillary length $\lambda_{ec} = K_3/\sigma_\|$ does not change much, being on the order of tens of micrometers. For pure DSCG, least-square fitting yields $\lambda_{ec} = (49 \pm 6)$ μm, while for DSCG+PEG mixtures, $\lambda_{ec} = (35 \pm 10)$ μm. We estimated $\sigma_\| \approx 10^{-6}$ J/m^2 for Col-I interface of a pure DSCG at $c = 0.47$ mol/kg by a spinning droplet technique [26], see Supplementary Material. With $\sigma_\| \approx 10^{-6}$ J/m^2, the fitted values of λ_{ec} suggest that K_3 in the C phase is within the range of 20-60 pN, which is reasonable since the highest measured value of K_3 in the N phase of DSCG is 50 pN [27].

The dimensionless parameter β defined in Eq. (2) and determined by the fitted λ_{ec} and experimental values of V, decreases as c and C increase; in the case of the DSCG+PEG mixture, $\beta \propto 1/C$, while the dependency is steeper with respect to c, Fig. 3b. According to Eq. (1), a smaller β means that a/r increases, which is intuitively clear. A smaller λ_{ec}, K_3 and β imply that the surface energy cost is high, thus the central hole shrinks to make the toroid more round and to reduce the interfacial area; the corresponding a/r is large. Larger λ_{ec} and β mean a higher K_3; the higher elastic cost of bend is relieved by expanding the central hole, i.e., by reducing a/r.

To summarize this section, the experiments uncover a rich morphology of Col toroids coexisting with the I phase. The shapes of toroids depend strongly on the concentration c of DSCG and concentration C of the crowding agent PEG and shows the following trends.

1) The cross-sections of the toroids are faceted because of hexagonal packing of the chromonic aggregates and anisotropy of the Col-I interfacial tension. The cross-section is not strictly hexagonal, with facets showing different lengths.

2) The volume V and the ratio of the minor radius a to the major radius r of toroids increase strongly with c and C. The central hole is large at low c and C, but shrinks towards a singular line with circular bend of columns at high concentrations.

3) A model of thin toroids that (i) assumes the interfacial tension to be independent of the orientation of the hexagonal lattice and (ii) neglects the contact with glass substrates, predicts that the ratio a/r increases when V increases or the elastocapillary length $\lambda_{ec} = K_3/\sigma_{\|}$ decreases. In liquid crystals the elastic energy of director gradients $K_3 V^{1/3}$ scales with the linear size $V^{1/3}$ of the system. Since the interfacial tension energy scales with the surface area, $\sigma_{\|} V^{2/3}$, the elastic energy prevails for small nuclei at low concentrations, producing skinny tori with a large central core. The interfacial surface tension prevails for large nuclei and high concentrations, yielding shapes close to spherical with a shrunk central hole; these could not be described by a simple model with $a \ll r$.

In the next section, we introduce a mathematical model of toroids that for any a/r accounts for anisotropy of the I-Col interfacial tension, faceted shapes, and surface tension at the glass substrate.

3. Modeling and Simulations

3.1. **A model of toroidal columnar nuclei**

Suppose that (ρ, ϕ, z) are cylindrical coordinates in $\mathbb{R}^3$ and let

$$\omega \subset \mathbb{R}^2_+ := \left\{(\rho, z) \subset \mathbb{R}^2 : \rho > 0\right\}$$

be a simply-connected domain in the right half of the ρz-plane. Let the Col nucleus Ω be axially symmetric (Fig. 4) and obtained by rotating ω around the z-axis,

$$\Omega := \left\{(\rho, \phi, z) \subset \mathbb{R}^3 : (\rho, z) \in \omega,\ \phi \in [0, 2\pi)\right\}.$$

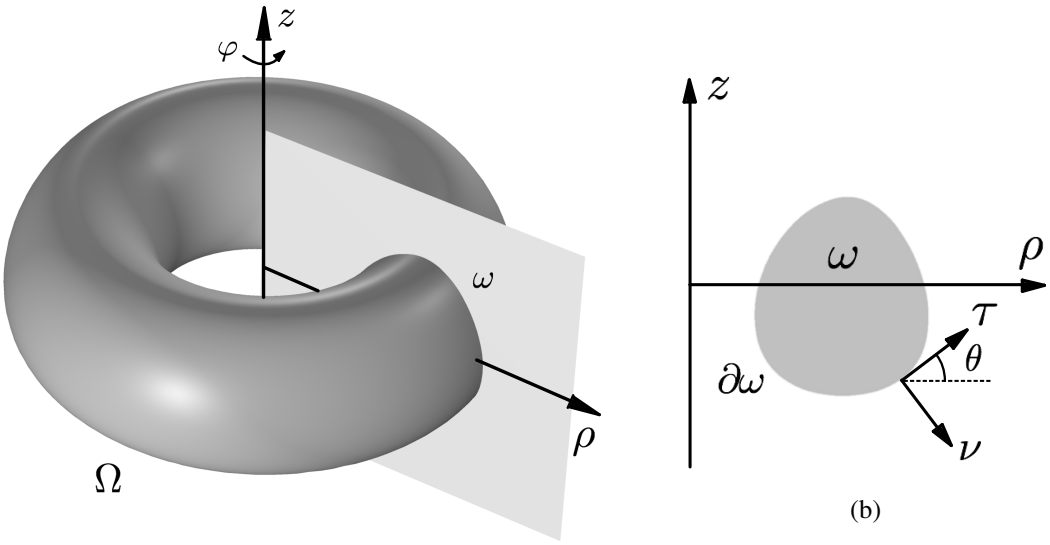

FIGURE 4. Geometry of the problem: (a) the toroidal Col nucleus Ω; (b) cross-section of Ω by a vertical plane gives a two-dimensional domain ω with the boundary $\partial\omega$.

The Col nucleus is composed of circularly bent "columns" centered on and lying in planes perpendicular to the z-axis. Each cross-section of the nucleus by a plane that contains the z-axis reveals a triangular lattice of points corresponding to the cross-sections of the columns; we assume that this lattice is fixed with one of the corresponding two-dimensional lattice vectors being parallel to the z-axis. The deformation of the chromonic columns is therefore limited to bending. The bending energy of a given column is proportional to the square of the column curvature so that

$$E_b := \frac{K_3}{2}\int_\Omega \rho^{-2} dV = \pi K_3 \int_\omega \rho^{-1} dA. \tag{3}$$

where $dV = \rho\, d\rho\, dz\, d\phi$ and $dA = d\rho\, dz$.

The Col-I interfacial tension depends on orientation of the columnar lattice vectors with respect to the surface normal. Because of the rotational invariance, the surface energy density can only depend on the relative angle between one of the lattice vectors and the surface normal. The outward normal to $\partial\Omega$ at a given point coincides with a normal at the same point to an appropriately rotated $\partial\omega$. It follows that the surface energy density is a function $\sigma : \mathbb{S}^2 \to \mathbb{R}$ of $\boldsymbol{\nu}$, where $\boldsymbol{\nu}$ is normal to both $\partial\Omega$ and $\partial\omega$. The surface energy of the columnar chromonic nucleus is then given by

$$E_s := \int_{\partial\Omega} \sigma(\boldsymbol{\nu}) dS = 2\pi \int_{\partial\omega} \sigma(\boldsymbol{\nu})\rho\, ds. \tag{4}$$

We seek the optimal shape of Col nuclei that minimizes the total energy functional

$$E[\omega] := E_b + E_s = \pi K_3 \int_\omega \rho^{-1} dA + 2\pi \int_{\partial\omega} \sigma(\boldsymbol{\nu})\rho\, ds, \tag{5}$$

among $\omega \subset \mathbb{R}^2_+$ that satisfy a fixed volume constraint $\mathrm{Vol}(\Omega) = V > 0$ or

$$V = 2\pi \int_\omega \rho\, dA. \tag{6}$$

We nondimensionalize the problem,

$$\tilde\rho = \frac{\rho}{V^{1/3}},\ \tilde z = \frac{z}{V^{1/3}},\ \tilde s = \frac{s}{V^{1/3}},\ \tilde\sigma = \frac{\sigma}{\sigma_\parallel},\ \tilde E = \frac{E}{\pi\sigma_\parallel V^{2/3}},$$

where $\sigma_{\|} > 0$ is a reference surface energy density. Then, dropping tildes and using the same symbols for the rescaled domain ω, we have

$$E[\omega] = \beta \int_{\omega} \rho^{-1} dA + 2 \int_{\partial\omega} \sigma(\boldsymbol{\nu}) \rho \, ds - 4\lambda \int_{\omega} \rho \, dA, \tag{7}$$

where the nondimensional β describes the relative contribution of the bulk bending and surface energies and λ is the Lagrange multiplier corresponding to the constraint (6).

Now suppose that the boundary curve

$$\partial\omega = \left\{ \mathbf{r}(s) = (\rho(s), z(s)) \in \mathbb{R}^2_+ : 0 \le s < L, \ \mathbf{r}(L) = \mathbf{r}(0), \ \mathbf{r}'(L) = \mathbf{r}'(0) \right\}$$

is positively oriented and parametrized with respect to the arc length s, where $L > 0$. Suppose further that $\mathbf{r}$ is smooth everywhere except for some $s = c$ where θ experiences a jump $[\theta]_{x=c} := \theta_+(c) - \theta_-(c) = \lim_{x\to c^+} \theta(x) - \lim_{x\to c^-} \theta(x)$. Here we define the orthonormal frame $(\boldsymbol{\tau}(s), \boldsymbol{\nu}(s))$ as

$$\boldsymbol{\tau}(s) = \mathbf{r}'(s) = (\cos\theta(s), \sin\theta(s)), \tag{8}$$

$$\boldsymbol{\nu}(s) = \mathbf{r}'_{\perp}(s) = (\sin\theta(s), -\cos\theta(s)), \tag{9}$$

where $\theta(s)$ is the angle between the tangent to the curve and the positive direction of the ρ-axis for all $s \in [0, L]$ and $\mathbf{a}_{\perp} = (a_2, -a_1)$ for every $\mathbf{a} = (a_1, a_2)$. Consider a general smooth variation $\delta\mathbf{r}$ of $\mathbf{r}$, then the same procedure as presented in Supplementary Material for smooth curves result in the following weak form of the Euler-Lagange equation

$$\int_0^L \left\{ \sigma(\boldsymbol{\nu}) \, \mathbf{e}_{\rho} \cdot \delta\mathbf{r} + \rho \left[\sigma(\boldsymbol{\nu}) \boldsymbol{\tau} - (\nabla\sigma(\boldsymbol{\nu}) \cdot \boldsymbol{\tau}) \, \boldsymbol{\nu} \right] \cdot \delta\mathbf{r}' \right\} ds + \beta \int_0^L \rho^{-1} \boldsymbol{\nu} \cdot \delta\mathbf{r} \, ds - 2\lambda \int_0^L \rho \boldsymbol{\nu} \cdot \delta\mathbf{r} \, ds = 0. \tag{10}$$

Standard arguments involving integration by parts, the strong form of the Euler-Lagrange equation, and continuity of the variation $\delta\mathbf{r}$ give the appropriate jump condition

$$\left[\sigma(\boldsymbol{\nu}) \boldsymbol{\tau} - (\nabla\sigma(\boldsymbol{\nu}) \cdot \boldsymbol{\tau}) \, \boldsymbol{\nu} \right]_{s=c} = 0, \tag{11}$$

or

$$\left[\gamma \boldsymbol{\tau} - \gamma_{\theta} \boldsymbol{\nu} \right]_{s=c} = 0, \tag{12}$$

when the condition is written in terms of

$$\gamma(\theta) := \sigma\left(\sin\theta, -\cos\theta\right).$$

Up to the definition of the orthonormal frame and the weight ρ, this corresponds to a standard condition of continuity of the capillary force

$$\mathbf{C}(\theta) = \rho \left(\gamma(\theta) \boldsymbol{\tau}(\theta) - \gamma_{\theta}(\theta) \boldsymbol{\nu}(\theta) \right) \tag{13}$$

across a corner [28].

To gain some insight into (12) we follow the exposition in [28] reviewed in Supplementary Material. Let $\mathbf{g}(\theta) = \gamma(\theta)^{-1} \boldsymbol{\nu}(\theta)$ be a Frank potential associated with the surface energy density γ. The polar plot of $\mathbf{g}$ is the so-called Frank diagram [29]. The *capillary force*

$$\mathbf{g}_{\theta}(\theta) = \frac{1}{\gamma^2(\theta)} \mathbf{C}(\theta),$$

is tangent to the Frank diagram. As demonstrated in [28], a range of angles $[\theta_-, \theta_+]$ corresponds to a corner if and only if the points $\mathbf{g}(\theta_-)$ and $\mathbf{g}(\theta_+)$ on the Frank diagram share a common tangent line (a Maxwell line).

The full problem for the unknown (ρ, θ, z, L) satisfied by the energy-minimizing curve is given by the system of ODEs

$$\begin{cases} \rho \left(\gamma_{\theta\theta} + \gamma \right) \theta' + \gamma \sin\theta + \gamma_{\theta} \cos\theta + \frac{\beta}{\rho} - 2\lambda\rho = 0, \\ \rho' = \cos\theta, \\ z' = \sin\theta, \end{cases} \tag{14}$$

subject to the conditions

$$\theta(L) = \theta(0) + 2\pi, \quad \theta'(L) = \theta'(0), \quad \int_0^L \cos\theta\, ds = \int_0^L \sin\theta\, ds = 0, \quad 2\pi \int_\omega \rho\, dA = 1, \tag{15}$$

as described in Supplementary Material.

In addition to considering full toroidal configurations, we also explore half-toroids attached to a glass substrate by considering the modified energy over ω, where

$$E_h[\omega] = \frac{\pi K_3}{2} \int_\omega \rho^{-1} dA + 2\sigma_g \int_\omega dA + \pi \int_{\partial\omega} \sigma(\boldsymbol{\nu})\rho\, ds, \tag{16}$$

among all ω for which the corresponding toroid Ω has a prescribed volume. Here σ_g is the surface energy density of a chromonics/glass interface. With a slight abuse of notation, the nondimensional expression for E_h is given by

$$E_h[\omega] = \frac{\beta}{2} \int_\omega \rho^{-1} dA + \frac{2\chi}{\pi} \int_\omega dA + \int_{\partial\omega} \sigma(\boldsymbol{\nu})\rho\, ds, \tag{17}$$

with the nondimensional parameter χ defined as

$$\chi = \frac{\sigma_g}{\sigma_\parallel}.$$

The system of Euler-Lagrange ODEs for (17) is similar to (14).

Next, we discuss behavior of solutions of (14)-(15). We use simulations to find stationary points of (7) via a gradient flow for this energy. In order to be able to simulate curves with corners, we use the standard regularization technique by adding a curvature-penalizing term to (7). The numerical scheme is described in the *Materials and Methods* section.

3.2. **Numerical results**

All simulations in this section were done using FELICITY [30]. We first simulate the shapes of toroids for the anisotropic surface tension

$$\sigma(\boldsymbol{\nu}) = \sigma_\parallel + \sigma_\parallel^a \sin^2(3\theta),$$

where the relationship between $\boldsymbol{\nu}$ and θ is given by (9). This expression can be rewritten in a nondimensional form

$$\gamma(\theta) = 1 + \gamma_1 \sin^2(3\theta), \tag{18}$$

where $\gamma_1 = \sigma_\parallel^a/\sigma_\parallel$.

Figs. 5a,b,c show the Frank diagram, Wulff plot, and Wulff construction, respectively, corresponding to (18) with $\gamma_1 = 0.2$ in the absence of bend elasticity. Note that the Frank diagram is not convex and there are six Maxwell lines that indicate that the equilibrium shape must have six facets and six corners. The Wulff construction in Fig. 5c produces shape that is close to the one obtained by accounting for both the surface tension and bend elasticity, when β is relatively large. For large β, the major radius r of the torus is large while its minor radius a is small in order to accommodate significant bending energy and the volume constraint. Because $a/r \ll 1$, the variation of ρ across the cross-section is smaller than ρ itself so that ρ is essentially constant. The shape of the cross-section in Fig. 5d is close to that obtained via the Wulff construction in Fig. 5c, however, the corners in the hexagon are rounded due to regularization employed in the gradient flow simulations. On the other hand, decreasing K_3 and β or increasing $\sigma_\parallel$ and volume, shrinks a wide "donut hole" into a narrow central core (Fig. 5e,f). We also observe that the corners and facets facing the z-axis become more rounded with decreasing β and the part of the curve closest to the z-axis transform into a large facet.

Changing the sign of γ_1 by setting $\gamma_1 = -0.2$ in (18) corresponds to rotating the plots in Fig. 5a,b,c by $\pi/3$, so that a facet faces the z-axis instead of a corner. Upon decreasing β and K_3 or increasing $S\sigma_\parallel$, in Fig. 5g,h,i this facet expands and approaches progressively closer to the z-axis.

Decreasing $|\gamma_1|$ produces produces a convex Frank diagram and less faceted shapes, Figs. S11-S14.

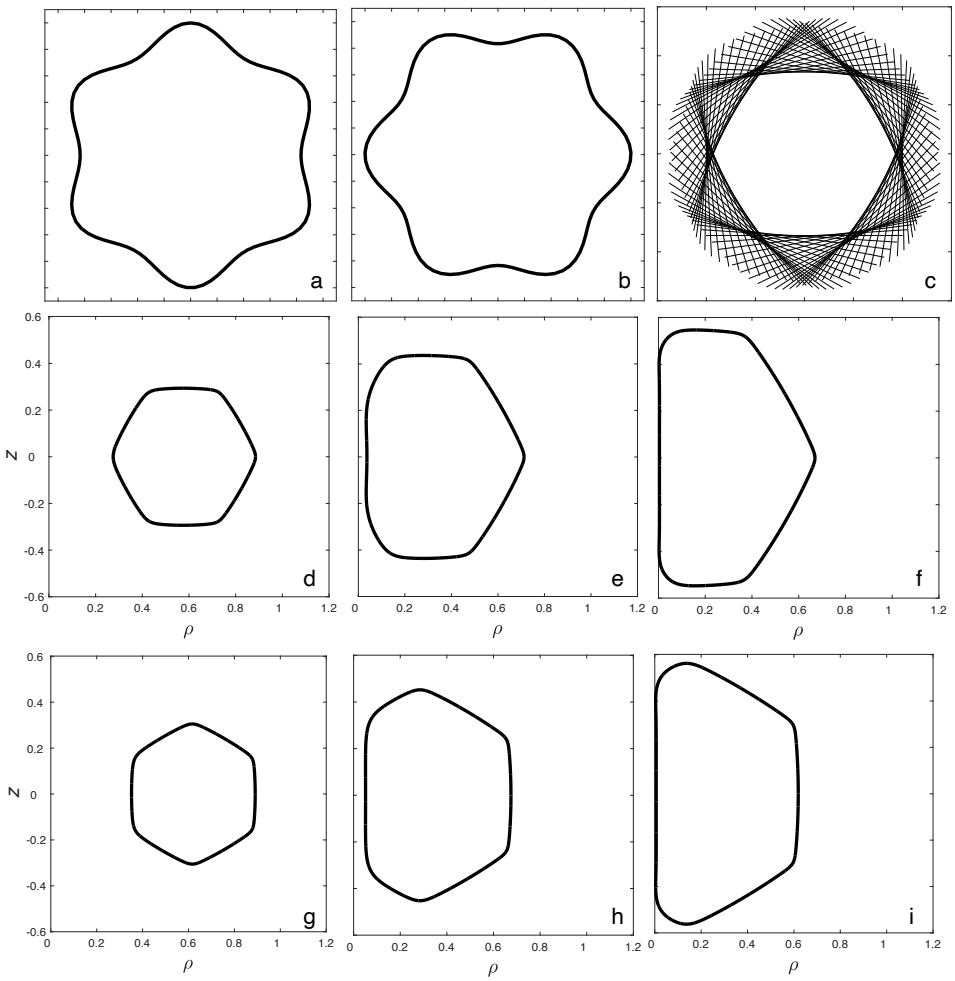

FIGURE 5. Numerical simulations of the toroidal shapes for the anisotropic interfacial energy $\gamma(\theta) = 1 + \gamma_1 \sin^2(3\theta)$ with $\gamma_1 = 0.2$ (a-f) and $\gamma_1 = -0.2$ (g-i); (a) Frank diagram; (b) Wulff plot; (c) Wulff construction; (d-f) cross-sections of toroids minimizing the sum of the elastic and interfacial energy for $\gamma_1 = 0.2$ where (d) $\beta = 1$, (e) $\beta = 0.1$, and (f) $\beta = 0.01$; (g-i) the same as in (d-f), but $\gamma_1 = -0.2$. In these simulations the regularization parameter $\varepsilon = 5\text{e-}4$ (See Section 5.2).

Fig. 6 demonstrates how the shape of *half-toroids* is influenced by the surface tension of the chromonic/substrate interface. Here we use gradient flow for the energy (22) to obtain equilibrium shapes. The interfacial I-Col energy for the director being normal to the I-Col interface is estimated (see Supplementary Material) to be larger than 10^{-4} N/m. Thus the dimensional glass-Col anchoring energy $\sigma_{\|}\chi$ must be lower than this number; a good starting estimate is 10^{-6} N/m, i.e., $|\chi|$ is on the order of 1. Qualitative argument in the Supplementary Material shows that χ might be either positive or negative. As χ increases, the principal radius of the toroid increases, while it becomes more "skinny", Fig. 6.

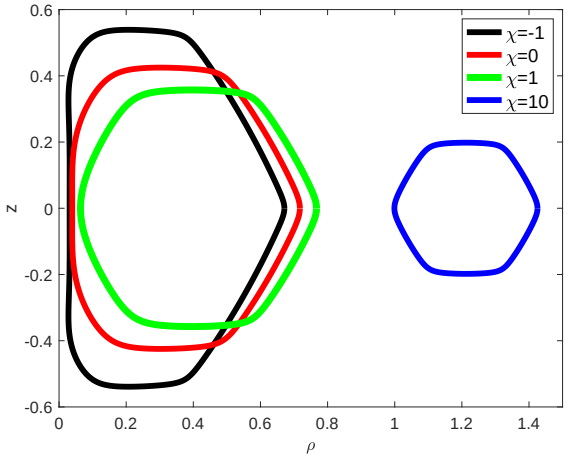

FIGURE 6. Cross-sections of the energy-minimizing half-toroids for the anisotropic surface energy $\gamma(\theta) = 1 + \gamma_1 \sin^2(3\theta)$ with $\gamma_1 = 0.2, \beta = 0.06$ and $\varepsilon = 10^{-3}$.

4. Discussion and Conclusions

The numerical model above captures well the faceted shapes of toroids. The sign of γ_1 defines qualitatively different shapes: $\gamma_1 < 0$ yields an outermost facet parallel to the axis of the nucleus, Fig. 5g,h,i, while $\gamma_1 > 0$ corresponds to two outer facets separated by a corner, Fig. 5d,e,f. In the experiment, pure DSCG shows a prevalence to form outermost facets parallel to the axis of the nucleus, Fig. 1a, while DSCG+PEG shows facets separated by a corner, Fig. 1f. The prevalence is not absolute, as in each case, the preferred shapes are observed with a probability of about 70%. It shows that both $\gamma_1 < 0$ and $\gamma_1 > 0$ correspond to the minima of the surface tension with only a small difference in the depth. We selected $\gamma_1 = -0.2$ for pure DSCG and $\gamma_1 = 0.2$ for DSCG+PEG as the best match with the facets observed experimentally.

Numerical simulations find the dimensionless shape parameters $a/V^{1/3}$, $r/V^{1/3}$, $R/V^{1/3}$, $b/V^{1/3}$, and $L/V^{1/3}$ as functions of β for fixed γ_1 and χ and the concentrations c and C. The numerical dependencies are compared to the experimental data to extract the matching β. These values are used to calculate the elastocapillary length $\lambda_{ec} = K_3/\sigma_{\|} = \beta V^{1/3}$ and to plot it as a function of c, Fig. 7a, and C, Fig. 7. Different shape parameters produce somewhat different values of β and λ_{ec}. In some cases, β could not be determined because the simulated shape parameters are outside of the range of positive-definite β. For this reason, $a/V^{1/3}$ data is not included in Fig. 7a. The scatter of data is natural since the experimental textures show a range of shapes even at the fixed c and C. The closest agreement of the experimental and numerical dependencies $\lambda_{ec}(c, C)$ is chosen to estimate γ_1 and χ. For DSCG, the closest correspondence is found for $\chi = -2.5$ and $\gamma_1 = -0.2$ as shown in Fig. 7. A departure from these values causes a disagreement between the simulations and the experiment; an example for $\chi = 1.0$ and $\gamma_1 = -0.2$ is illustrated in Supplementary Material, Fig. S4a. For DSCG+PEG, the simulation matches the experiments best (Fig. 7b) when $\chi = 1.1$ and $\gamma_1 = 0.2$. When χ departs from this value, the discrepancy grows; see Supplementary Material, Fig. S4b for $\chi = -4.5$ and $\gamma_1 = 0.2$. The values $\chi = -2.5$ and 1.1 are within the expected range, as discussed in the Supplement S2, see Supplementary Material, Fig. S3.

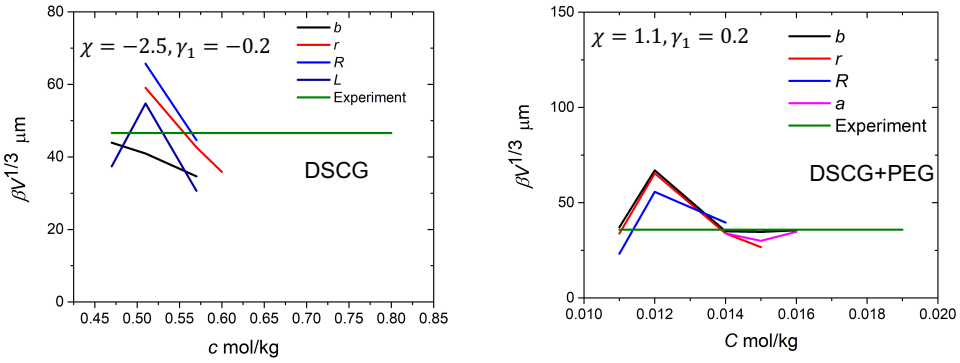

a b

FIGURE 7. Comparison of simulated $\beta V^{1/3}$ to the experimentally obtained values for (a) pure DSCG and (b) DSCG+PEG. The best match between the simulations and the experimental results is achieved when $\chi = -2.5$ and $\gamma_1 = -0.2$ for pure DSCG and $\chi = 1.1$ and $\gamma_1 = 0.2$ for DSCG+PEG.

In conclusion, we described the unusual faceted toroidal shapes of the columnar nuclei coexisting with the isotropic phase of a lyotropic chromonic liquid crystal. The shapes are reminiscent of the DNA condensates but occur at a much larger scale, suitable for optical microscopy observation. Experiments show that the toroidal shapes depend strongly on the concentration of the chromonic molecules in the aqueous solutions. Theoretical and numerical analysis demonstrates that the faceted shapes result from the anisotropy of the interfacial tension, associated with different orientations of the hexagonal lattice at the interface. The facets are not equal in length, as the ones closer to the center of toroids tend to be elongated more than the facets farther away from the center. Numerical simulations demonstrate that the bending elasticity of the columns is the primary cause of this behavior. The balance of bending energy with the elastic constant K_3 and anisotropic interfacial energy $\sigma_{\|}$, expressed as the elastocapillary length $\lambda_{ec} = K_3/\sigma_{\|}$ controls the width of the central opening of the toroids, which in the experiments varies from tens of micrometers to submicrometer. Larger openings and skinny toroids, observed at low concentrations of the chromonic molecules and crowding agent, are facilitated by a smaller interfacial tension $\sigma_{\|}$, smaller volume of the nuclei and a larger bend constant K_3, while the opposite behavior with toroids approaching faceted spheres, is observed at high concentrations. Although the experiments were performed for half-toroids attached to the glass plates of the cells, the general trends are expected to be the same for full toroids.

5. MATERIALS AND METHODS

5.1. **Experiments**

Disodium cromoglycate (DSCG), Fig. S1, with a purity of 98% was purchased from Alfa Aesar and used without further purification. De-ionized water with resistivity ≥ 18.0 MΩcm was used to prepare the aqueous solutions of DSCG. At 25°C, a homogeneous nematic (N) phase appears when the concentration of DSCG, c, is in the range of $0.3 \leq c \leq 0.65$ mol/kg ($13.5 \leq c \leq 25$ wt%). In the range $0.65 \leq c \leq 0.70$ mol/kg ($25 \leq c \leq 26.5$ wt%), the nematic + columnar (N+Col) coexistence region appears, and at $c > 0.70$ mol/kg, the solution is in the homogeneous columnar (Col) phase [31]. At T=45°C , the solution remains in the I phase when $c \leq 0.40$ mol/kg (≤17wt%); above this concentration, the Col and I phases coexist. The liquid crystalline regions exhibit a higher DSCG concentration compared to the overall concentration in the entire sample [6, 32, 33, 20]. Fig. S1 schematizes the molecular arrangements within the aggregates and their mutual alignments in the I, N, and Col phases.

Addition of the crowding agent PEG to aqueous solutions of DSCG expands the temperature range of the biphasic regions and condenses Col nuclei, Fig. S2. For example, an isotropic DSCG solution with $c = 0.34$ mol/kg (15 wt%) at 45°C transforms into a biphasic I+Col state when PEG is added at the concentrations $C = (0.03 - 0.07)$ mol/kg [6, 20]. We use PEG with a molecular weight of 3.35 kg/mol (Sigma Aldrich). The gyration diameter of the PEG molecules $2r_g \approx 4.4$ nm is larger than the inter-columnar separation $\approx (1.9 - 3.2)$ nm in the columnar phase of DSCG [9, 6]. The PEG molecules are thus expelled from the liquid crystalline regions and partition into the isotropic regions [6].

The facets of toroids are best observed when the axis of rotational symmetry are in the plane of the view. A tangential alignment of the director $\widehat{\mathbf{n}}$ at bounding plates does not allow one to observe the faceted structures clearly. Because of this, we use clean glass rectangular capillaries (purchased from VitroCom) that yield a homeotropic alignment after cleaning in an ultrasonic bath for 15 minutes at 60°C followed by an isopropanol rinse and drying in an oven for 10 min at 80°C. The capillaries are 0.2 mm thick and 4.0 mm wide. After filling with the LC, the two ends of the capillary are sealed with an epoxy glue to prevent evaporation of water. The samples are placed inside a hot stage (Linkam Model PE94) and observed using an optical polarizing microscope (Nikon Optiphot 2 POL) in the transmission mode with parallel polarizers. The materials are cooled down from the homogeneous I phase to the biphasic I+Col region at a rate of 0.1°C/min and then the temperature of the sample is fixed, either 45°C (DSCG samples) or at 42°C (DSCG+PEG). The Col nuclei form half-toroidal handles, Figs. 1, S2, attached to the bottom glass plate of the capillary as shown in Fig. 1c since their mass density is higher than that of the I phase [6]. The Col nuclei were explored 20 min after the cooling stopped and the temperature fixed, to ensure that they have reached their stationary state.

5.2. **Numerical method**

5.2.1. Computing energy minimizers via gradient flow for the regularized energy. We seek to minimize the energy $E[\omega] = 2\pi J[\omega]$ over ω where

$$J[\omega] = \frac{\beta}{2}\int_\omega \rho^{-1} dA + \int_{\partial\omega} \sigma(\boldsymbol{\nu})\rho\, ds + \frac{\varepsilon}{2}\int_{\partial\omega} \kappa^2\, ds, \tag{19}$$

subject to the constraint that the volume is fixed; note that $\varepsilon \geq 0$ is a regularization parameter. The associated Lagrangian is

$$\mathcal{L}[\omega, \lambda] = J[\omega] + \lambda\left(C_v - \int_\omega \rho dA\right), \tag{20}$$

where $C_v > 0$ is the desired volume (without the factor of 2π).

Note that one can rewrite (20) entirely in terms of $\Gamma := \partial\omega$. By Gauss' divergence theorem (in the plane), we have

$$\int_\omega \rho^{-1}\, dA = \int_\Gamma (\boldsymbol{\nu}\cdot\mathbf{e}_1)\log\rho\, ds, \qquad \int_\omega \rho\, dA = \frac{1}{2}\int_\Gamma (\boldsymbol{\nu}\cdot\mathbf{e}_1)\rho^2\, ds. \tag{21}$$

Therefore, $J[\omega] \equiv J[\Gamma]$ and $\mathcal{L}[\omega, \lambda] \equiv \mathcal{L}[\Gamma, \lambda]$.

For the energy of half-toroids introduced in (17), the associated relaxed energy can be written as

$$J_h[\omega] = \frac{\beta}{2}\int_\omega \rho^{-1} dA + \frac{2\chi}{\pi}\int_\omega dA + \int_{\partial\omega} \sigma(\boldsymbol{\nu})\rho\, ds + \frac{\varepsilon}{2}\int_{\partial\omega} \kappa^2\, ds, \tag{22}$$

with the Lagrangian given by

$$\mathcal{L}_h[\omega, \lambda] = J_h[\omega] + \lambda\left(C_v - \int_\omega \rho dA\right), \tag{23}$$

where $C_v > 0$ is the desired volume (without the factor of 2π). One can still rewrite (23) entirely in terms of $\Gamma := \partial\omega$ because

$$\int_\omega dA = \int_\Gamma (\boldsymbol{\nu}\cdot\mathbf{e}_1)\rho\, ds. \tag{24}$$

Therefore, $J_h[\omega] \equiv J[\Gamma]$ and $\mathcal{L}_h[\omega, \lambda] \equiv \mathcal{L}_h[\Gamma, \lambda]$.

5.2.2. Gradient Flow. Since the first-order conditions for a critical point of (20) are non-linear, we use a gradient flow strategy to find the minimizer. Suppose $\mathbf{X}$ is a parameterization of Γ that depends on a pseudo-time variable t. In other words, $\Gamma(t)$ is time-varying and is parameterized (instantaneously) by $\mathbf{X}(\cdot, t)$. Hence, our goal is to create a "velocity" $\mathbf{V} = \partial_t \mathbf{X}$ so that the energy $J[\Gamma(t)]$ is monotonically decreasing and $\partial_t \int_{\omega(t)} \rho dA = 0$ (volume is preserved).

We achieve this energy decrease by a gradient flow, i.e. we define $\mathbf{V}$ to be minus the "shape gradient" of (20) with a (time-varying) Lagrange multiplier that enforces volume conservation. The next section describes this more specifically.

5.2.3. Weak Formulation. We assume that, for each t, $\mathbf{V}(t)$ is defined on $\Gamma(t)$ and lies in a Hilbert space $\mathcal{H} = \mathcal{H}(t)$. Let $\langle \mathbf{V}, \mathbf{Y} \rangle$ be an inner product on $\mathcal{H}$ for any functions $\mathbf{V}, \mathbf{Y} \in \mathcal{H}$. With this, we define the gradient flow weakly, i.e. $\mathbf{V}(t)$ solves (for each t)

$$\langle \mathbf{V}, \mathbf{Y} \rangle = -\delta_\Gamma \mathcal{L}[\Gamma(t), \lambda(t); \mathbf{Y}], \tag{25}$$

for all admissible "shape" perturbations $\mathbf{Y}$. Here, δ_Γ denotes the shape derivative, which is explained in [34, 35]. Combining (25) with the boundary motion equation:

$$\frac{d}{dt}\mathbf{X} = \mathbf{V}(\mathbf{x}, t), \quad \text{for all } \mathbf{X} \in \Gamma(t), \tag{26}$$

completely defines the evolution of the boundary $\Gamma(t)$. For example, if $J[\Gamma] = \int_\Gamma 1$, then the evolution would simply be mean curvature flow: $\mathbf{V} = -\kappa \boldsymbol{\nu}$.

5.2.4. Fully Discrete Approximation. In order to have a tractable problem, we discretize (25) with a variant of a method found in [36, 37, 38]. We first discretize the curve Γ by a polygonal curve. Hence, $\mathbf{X}$ is a vector-valued, continuous piecewise linear finite element function [39, 40]. In addition, we use a backward-Euler method for approximating (26) with a fixed time step δt. Therefore, given the current guess for the polygonal curve $\mathbf{X}^m$ (at time index m), we introduce the continuous piecewise linear finite element space $\mathbb{V}^m$ defined on Γ^m. Thus, $\mathbf{X}^m \in [\mathbb{V}^m]^2$, which is a vector valued finite element space.

The polygonal curve at the next time index is obtained by solving the following system of equations, i.e. find $(\kappa_\sigma^{m+1}, \kappa^{m+1}, \mathbf{X}^{m+1}, \lambda^{m+1})$ such that:

$$\begin{aligned} \left\langle \frac{\mathbf{X}^{m+1} - \mathbf{X}^m}{\delta t}, \boldsymbol{\nu}_h^m \eta \right\rangle_m^h + \left\langle \kappa_\sigma^{m+1}, \eta \right\rangle_m^h + \varepsilon \left\langle \partial_s \kappa^{m+1}, \partial_s \eta \right\rangle_m \\ - \lambda^{m+1} \langle \rho, \eta \rangle_m^h = \frac{\varepsilon}{2} \left\langle (\kappa^m)^3, \eta \right\rangle_m^h, \ \forall \eta \in \mathbb{V}^m, \end{aligned} \tag{27}$$

$$\begin{aligned} \left\langle \kappa_\sigma^{m+1}, \boldsymbol{\nu}_h^m \cdot \mathbf{Y} \right\rangle_m^h - \left\langle \rho\sigma(\boldsymbol{\nu}^m)\partial_s \mathbf{X}^{m+1}, \partial_s \mathbf{Y} \right\rangle_m - \frac{\beta}{2} \left\langle \rho^{-2}(\mathbf{X}^{m+1} \cdot \mathbf{e}_1), \mathbf{Y} \cdot \boldsymbol{\nu}^m \right\rangle_m \\ - \frac{2\chi}{\pi} \langle 1, \mathbf{Y} \cdot \boldsymbol{\nu}^m \rangle_m = -\langle \rho(\boldsymbol{\nu} \cdot \partial_s \mathbf{Y})\boldsymbol{\tau} \cdot \sigma'(\boldsymbol{\nu}^m), 1 \rangle_m + \langle \sigma(\boldsymbol{\nu}^m)(\mathbf{Y} \cdot \mathbf{e}_1), \eta \rangle_m^h, \ \forall \mathbf{Y} \in [\mathbb{V}^m]^2, \end{aligned} \tag{28}$$

$$\left\langle \kappa^{m+1}, \boldsymbol{\nu}_h^m \cdot \mathbf{Y} \right\rangle_m^h - \left\langle \partial_s \mathbf{X}^{m+1}, \partial_s \mathbf{Y} \right\rangle_m = 0, \ \forall \mathbf{Y} \in [\mathbb{V}^m]^2, \tag{29}$$

$$-\left\langle \frac{\mathbf{X}^{m+1} - \mathbf{X}^m}{\delta t}, \boldsymbol{\nu}_h^m \rho \right\rangle_m^h = \frac{1}{\delta t} \left[\int_{\omega^m} \rho dA - C_v \right], \tag{30}$$

where $\langle \cdot, \cdot \rangle_m$ denotes the inner product on Γ^m, $\langle \cdot, \cdot \rangle_m^h$ is a mass lumped inner product on Γ^m, and $\boldsymbol{\nu}_h^m$ is a "discrete" vertex normal vector of Γ^m. The system (27)-(30) is linear and *semi-implicit* which allows for taking large time steps (see [36, 37, 38] with the caveat about anisotropic surface energy and the regularization parameter).

The first equation, (27), is an approximation of the gradient descent equation (25). Equation (29) is essentially a "weak" definition of the standard curvature of Γ^{m+1} (viewed as a planar curve), whereas (28)

is a weak definition of the "anisotropic, radially weighted" curvature. The last equation accounts for the volume constraint, whose right-hand-side corrects for any deviations from the desired volume C_v.

After solving the system, we obtain $\mathbf{X}^{m+1}$ which is defined on Γ^m. We obtain the new curve Γ^{m+1} by simply taking the nodal values of $\mathbf{X}^{m+1}$ as the new vertex positions of the polygonal curve.

Therefore, given an initial curve Γ^0, we obtain Γ_m by iteratively solving the above system m times. This requires an initial guess for κ^0 because it appears in the right-hand-side of (27). This is accomplished by using a similar equation to (29). More specifically, we find $\mathbf{K}^0 \in [\mathbb{V}^0]^2$ such that

$$\left\langle \mathbf{K}^0, \mathbf{Y} \right\rangle_0^h = \left\langle \partial_s \mathbf{X}^0, \partial_s \mathbf{Y} \right\rangle_0, \ \forall \mathbf{Y} \in [\mathbb{V}^0]^2, \tag{31}$$

and then computing $\kappa^0(\mathbf{x}_i) := \boldsymbol{\nu}_h^m(\mathbf{x}_i) \cdot \mathbf{K}^0(\mathbf{x}_i)$ at each vertex $\mathbf{x}_i$ in Γ^0.

6. Acknowledgments

This work was supported by NSF grants DMS-2106675 (ODL), DMS-2106551 (DG), DMS-1555222-CAREER and DMS-2111474 (SWW), DMS-1435372, DMS-1729589 and DMS-1816740 (MCC). The authors would like to thank Dr. Thomas A. Everett from the Enhanced Oil Recovery Lab at Purdue University for his help using the spinning drop tensiometer. MCC also aknowledges the hospitality of the Isaac Newton Institute at Cambridge University, UK and the support from the Simons Foundation.

References

[1] G. Friedel, "Les états mésomorphes de la matière," *Annales de Physique*, vol. 9, no. 18, pp. 273–474, 1922.

[2] J. D. Bernal and I. Fankuchen, "X-ray and crystallographic studies of plant virus preparations: I. introduction and preparation of specimens ii. modes of aggregation of the virus particles," *The Journal of General Physiology*, vol. 25, no. 1, pp. 111–146, 1941.

[3] W.-S. Wei, Y. Xia, S. Ettinger, S. Yang, and A. Yodh, "Molecular heterogeneity drives reconfigurable nematic liquid crystal drops," *Nature*, vol. 576, no. 7787, pp. 433–436, 2019.

[4] K. Peddireddy, S. Čopar, K. V. Le, I. Muševič, C. Bahr, and V. S. Jampani, "Self-shaping liquid crystal droplets by balancing bulk elasticity and interfacial tension," *Proceedings of the National Academy of Sciences*, vol. 118, no. 14, 2021.

[5] O. D. Lavrentovich and Yu. A. Nastishin, "Division of drops of a liquid-crystal in the case of a cholesteric–smectic-a phase-transition," *JETP Lett*, vol. 40, no. 6, pp. 1015–1019, 1984.

[6] L. Tortora, H.-S. Park, S.-W. Kang, V. Savaryn, S.-H. Hong, K. Kaznatcheev, D. Finotello, S. Sprunt, S. Kumar, and O. D. Lavrentovich, "Self-assembly, condensation, and order in aqueous lyotropic chromonic liquid crystals crowded with additives," *Soft Matter*, vol. 6, no. 17, pp. 4157–4167, 2010.

[7] J. Lydon, "Chromonic review," *Journal of Materials Chemistry*, vol. 20, no. 45, pp. 10071–10099, 2010.

[8] J. Lydon, "Chromonic liquid crystalline phases," *Liquid Crystals*, vol. 38, no. 11-12, pp. 1663–1681, 2011.

[9] H.-S. Park and O. D. Lavrentovich, "Lyotropic chromonic liquid crystals: Emerging applications," *Liquid crystals beyond displays: chemistry, physics, and applications*, pp. 449–484, 2012.

[10] P. J. Collings, J. N. Goldstein, E. J. Hamilton, B. R. Mercado, K. J. Nieser, and M. H. Regan, "The nature of the assembly process in chromonic liquid crystals," *Liquid Crystals Reviews*, vol. 3, no. 1, pp. 1–27, 2015.

[11] S.-W. Tam-Chang and L. Huang, "Chromonic liquid crystals: properties and applications as functional materials," *Chemical communications*, no. 17, pp. 1957–1967, 2008.

[12] J. Jeong, Z. S. Davidson, P. J. Collings, T. C. Lubensky, and A. Yodh, "Chiral symmetry breaking and surface faceting in chromonic liquid crystal droplets with giant elastic anisotropy," *Proceedings of the National Academy of Sciences*, vol. 111, no. 5, pp. 1742–1747, 2014.

[13] M. Stukan, V. Ivanov, A. Y. Grosberg, W. Paul, and K. Binder, "Chain length dependence of the state diagram of a single stiff-chain macromolecule: Theory and monte carlo simulation," *The Journal of chemical physics*, vol. 118, no. 7, pp. 3392–3400, 2003.

[14] N. V. Hud and I. D. Vilfan, "Toroidal DNA condensates: unraveling the fine structure and the role of nucleation in determining size," *Annu. Rev. Biophys. Biomol. Struct.*, vol. 34, pp. 295–318, 2005.

[15] G. Maurstad and B. T. Stokke, "Toroids of stiff polyelectrolytes," *Current opinion in colloid & interface science*, vol. 10, no. 1-2, pp. 16–21, 2005.

[16] A. Leforestier and F. Livolant, "Structure of toroidal DNA collapsed inside the phage capsid," *Proceedings of the National Academy of Sciences*, vol. 106, no. 23, pp. 9157–9162, 2009.

[17] M.-L. Ainalem and T. Nylander, "DNA condensation using cationic dendrimers—morphology and supramolecular structure of formed aggregates," *Soft Matter*, vol. 7, no. 10, pp. 4577–4594, 2011.

[18] K. Osada, "Versatile DNA folding structures organized by cationic block copolymers," *Polymer Journal*, vol. 51, no. 4, pp. 381–387, 2019.
[19] M. Kleman and O. D. Laverntovich, *Soft matter physics: an introduction*. New York: Springer-Verlag, 2003.
[20] R. Koizumi, B.-X. Li, and O. D. Lavrentovich, "Effect of crowding agent polyethylene glycol on lyotropic chromonic liquid crystal phases of disodium cromoglycate," *Crystals*, vol. 9, no. 3, p. 160, 2019.
[21] Y. Bouligand, "Geometry of (non smectic) hexagonal mesophases," *Journal de Physique*, vol. 41, no. 11, pp. 1297–1306, 1980.
[22] P. Oswald, "Observations in homeotropic anchoring of the+ π disclinations in a hexagonal discotic liquid crystal," *Journal de Physique Lettres*, vol. 42, no. 8, pp. 171–173, 1981.
[23] V. G. Nazarenko, O. P. Boiko, H. S. Park, O. M. Brodyn, M. M. Omelchenko, L. Tortora, Y. A. Nastishin, and O. D. Lavrentovich, "Surface alignment and anchoring transitions in nematic lyotropic chromonic liquid crystal," *Physical Review Letters*, vol. 105, no. 1, p. 017801, 2010.
[24] S. Zhou, O. Tovkach, D. Golovaty, A. Sokolov, I. S. Aranson, and O. D. Lavrentovich, "Dynamic states of swimming bacteria in a nematic liquid crystal cell with homeotropic alignment," *New Journal of Physics*, vol. 19, no. 5, p. 055006, 2017.
[25] P. C. Mushenheim, R. Trivedi, S. Roy, M. Arnold, D. Weibel, and N. Abbott, "Effects of confinement, surface-induced orientation and strain on dynamic behavior of bacteria in thin liquid crystalline films," *Soft Matter*, vol. 11, pp. 6821–6831, 2015.
[26] B. Vonnegut, "Rotating bubble method for the determination of surface and interfacial tensions," *Review of Scientific Instruments*, vol. 13, no. 1, pp. 6–9, 1942.
[27] S. Zhou, K. Neupane, Y. A. Nastishin, A. R. Baldwin, S. V. Shiyanovskii, O. D. Lavrentovich, and S. Sprunt, "Elasticity, viscosity, and orientational fluctuations of a lyotropic chromonic nematic liquid crystal disodium cromoglycate," *Soft Matter*, vol. 10, pp. 6571–6581, 2014.
[28] S. Angenent and M. E. Gurtin, "Multiphase thermomechanics with interfacial structure. 2. Evolution of an isothermal interface," *Archive for Rational Mechanics and Analysis*, vol. 108, pp. 323–391, Nov 1989.
[29] F. Frank, "Metal surfaces: structure, energetics and kinetics," *American Society for Metals, Ohio*, p. 1, 1963.
[30] S. W. Walker, "Felicity: A matlab/c++ toolbox for developing finite element methods and simulation modeling," *SIAM Journal on Scientific Computing*, vol. 40, no. 2, pp. C234–C257, 2018.
[31] N. Zimmermann, G. Jünnemann-Held, P. J. Collings, and H.-S. Kitzerow, "Self-organized assemblies of colloidal particles obtained from an aligned chromonic liquid crystal dispersion," *Soft Matter*, vol. 11, no. 8, pp. 1547–1553, 2015.
[32] T. L. Madden and J. Herzfeld, "Exclusion of spherical particles from the nematic phase of reversibly assembled rod-like particles," *MRS Online Proceedings Library*, vol. 248, no. 1, pp. 95–100, 1991.
[33] T. L. Madden and J. Herzfeld, "Liquid crystal phases of self-assembled amphiphilic aggregates," *Philosophical Transactions of the Royal Society of London. Series A: Physical and Engineering Sciences*, vol. 344, no. 1672, pp. 357–375, 1993.
[34] M. C. Delfour and J.-P. Zolésio, *Shapes and Geometries: Analysis, Differential Calculus, and Optimization*, vol. 4 of *Advances in Design and Control*. SIAM, 2nd ed., 2011.
[35] S. W. Walker, *The Shapes of Things: A Practical Guide to Differential Geometry and the Shape Derivative*, vol. 28 of *Advances in Design and Control*. SIAM, 1st ed., 2015.
[36] J. W. Barrett, H. Garcke, and R. Nürnberg, "A parametric finite element method for fourth order geometric evolution equations," *Journal of Computational Physics*, vol. 222, no. 1, pp. 441 – 467, 2007.
[37] J. W. Barrett, H. Garcke, and R. Nürnberg, "Parametric approximation of willmore flow and related geometric evolution equations," *SIAM Journal of Scientific Computing*, vol. 31, no. 1, pp. 225–253, 2008.
[38] J. W. Barrett, H. Garcke, and R. Nürnberg, "A variational formulation of anisotropic geometric evolution equations in higher dimensions," *Numerische Mathematik*, vol. 109, no. 1, pp. 1–44, 2008.
[39] J. Alberty, C. Carstensen, and S. A. Funken, "Remarks around 50 lines of MATLAB: Short finite element implementation," *Numerical Algorithms*, vol. 20, pp. 117–137, 1998.
[40] S. C. Brenner and L. R. Scott, *The Mathematical Theory of Finite Element Methods*, vol. 15 of *Texts in Applied Mathematics*. New York, NY: Springer, 3rd ed., 2008.

Advanced Materials and Liquid Crystal Institute, Materials Science Graduate Program, Kent State University, Kent, OH 44242, USA
Email address: rkoizumi@kent.edu

Department of Mathematics, The University of Akron, Akron, OH 44325-4002
Email address: dmitry@uakron.edu

Advanced Materials and Liquid Crystal Institute, Department of Physics, Kent State University, Kent, OH 44242, USA and Department of Physics, University of Bisha, Bisha, 67714, Saudi Arabia
Email address: aalqarn1@kent.edu

Department of Mathematics, Louisiana State University, Baton Rouge, LA 70803-4918
Email address: walker@lsu.edu

Advanced Materials and Liquid Crystal Institute, Kent State University, Kent, OH 44242, USA and Hetman Petro Sahaidachnyi National Army Academy, 32 Heroes of Maidan street, Lviv, 79012, Ukraine
Email address: nastyshyn_yuriy@yahoo.com

School of Mathematics, University of Minnesota, Minneapolis, MN 55455, USA
Email address: calde014@umn.edu

Advanced Materials and Liquid Crystal Institute, Materials Science Graduate Program, Kent State University, Kent, OH 44242, USA and Department of Physics, Kent State University, Kent, Ohio 44242, USA
Email address: olavrent@kent.edu